



Research paper

Local coulomb attraction for enhanced H₂ evolution stability of metal sulfide photocatalysts

Jun Jie Zhao^a, Yu Hang Li^a, Peng Fei Liu^a, Yu Lei Wang^a, Xu Lei Du^a, Xue Lu Wang^a,
Hui Dan Zeng^c, Li Rong Zheng^b, Hua Gui Yang^{a,*}

^a Key Laboratory for Ultrafine Materials of Ministry of Education, School of Materials Science and Engineering, East China University of Science and Technology, 130 Meilong Road, Shanghai 200237, China

^b Beijing Synchrotron Radiation Facility, Institute of High Energy Physics, Chinese Academy of Sciences, Beijing 100049, China

^c School of Materials Science and Engineering, East China University of Science and Technology, 130 Meilong Road, Shanghai 200237, China

ARTICLE INFO

Keywords:

Hydrogen evolution
Local coulomb attraction
Metal sulfides
Photocatalytic stability

ABSTRACT

Cadmium sulfide (CdS) is considered as a promising semiconductor photocatalyst for its outstanding light absorbance and photoinduced charge separation, but it suffers from severe photocorrosion, mainly due to the sluggish kinetics of holes transfer. In this work, we introduce the strong local Coulomb attraction, which is demonstrated via the in situ K-edge X-ray absorption near edge (XANES) analysis, to accelerate the migration of holes for long-term photocatalytic activity. As a proof-of-concept sample, the hole-attraction Fe₂O₃/CdS nanorods evidence an outstanding stability of at least 6 days without obvious deactivation, and feature with an excellent H₂ evolution rate of 20.7 mmol g⁻¹ h⁻¹. Moreover, this Coulomb attraction strategy can be leveraged to enhance the photocatalytic performance of Zn_{0.5}Cd_{0.5}S, indicating the wide application of the strategy.

1. Introduction

Developing high-activity and robust-stability photocatalysts for water splitting to hydrogen (H₂) as an excellent substitution for fossil fuels, has been a challenging and crucial research topic to overcome the serious environmental issues and increasing energy demand [1–4]. Cadmium sulfide (CdS) with a narrow band gap of ~2.4 eV, has attracted much attention over the past few decades in this research field [5,6], due to its suitable energy band position and the efficient generation of photoinduced electron-hole pairs [7,8]. However, the poor photocatalytic stability largely limits its further applications, because of the undesirable photocorrosion that excess holes induce the rapid oxidation of crystal lattice S²⁻ ions to form S⁰ phase [9]. Worse while, the sluggish kinetics of holes transfer aggravates this conundrum, causing the oxidation of crystal lattice S²⁻ rather than H₂O or sacrificial agent on the CdS surface. Therefore, it is of great importance to accelerate the photoinduced holes migration away from crystal lattice, thus enhancing CdS photostability [10].

Efforts have been devoted to improving CdS photocatalytic stability in the past few years. For example, constructing Z-scheme systems and heterogeneous structures via integrating CdS with other photocatalysts such as TiO₂ [11–13], WO₃ [14,15], ZnO [16–18], ZnS [19,20] and PdS [21–23] are effective strategies to facilitate the holes transfer driven by

potential difference. Furthermore, sacrificial electron donors are used to fast remove holes from CdS crystal for long-term photocatalytic activity [24,25], mainly including lactic acid [26–28], Na₂SO₃/Na₂S [29–31] and alcohols [32,33]. However, the durability of most CdS based photocatalysts is still far below 100 h. In addition, other metal sulfides suffer from this problem equally, while no versatile strategy can be employed to efficiently overcome this common issue. The Coulomb attraction is considered as a universal signature between positive and negative charges, which is a key impact to determine charges behaviors. According to this law, the direction and rate of hole and electron transfer can be controlled under their mutual Coulomb attraction. Thus, we anticipate a versatile strategy of Coulomb force to explain and design the process of fast holes transfer for improving the photocatalytic stability of metal sulfides.

Herein, we employ the strong local Coulomb attraction to rapidly attract the photogenerated holes in metal sulfides from bulk crystal lattice to surface oxidation sites. As a proof-of-concept sample, the hole-attraction Fe₂O₃ nanoparticles (NPs) were loaded on the CdS nanorods (NRs) surface via a facile photochemical metal-organic deposition (PMOD). The photocatalytic durability is dramatically enhanced, over 6 days with H₂ evolution rate of 20.7 mmol g⁻¹ h⁻¹. The in situ K-edge X-ray absorption near edge (XANES) analysis demonstrates the existence of local Coulomb attraction. The principle of Coulomb attraction

* Corresponding author.

E-mail address: hgyang@ecust.edu.cn (H.G. Yang).

<http://dx.doi.org/10.1016/j.apcatb.2017.09.012>

Received 22 June 2017; Received in revised form 29 August 2017; Accepted 5 September 2017

Available online 06 September 2017

0926-3373/ © 2017 Elsevier B.V. All rights reserved.

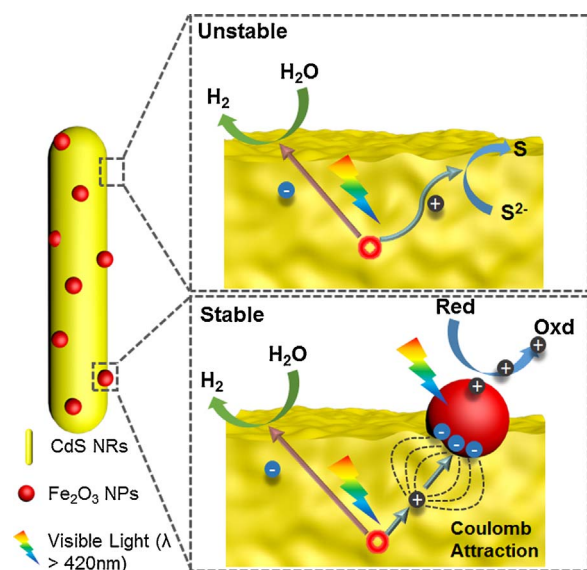


Fig. 1. Schematic illustration of Coulomb attraction strategy. The oxidation process of S^{2-} exist in the pure CdS under illumination, causing poor photocatalytic stability. After Fe_2O_3 NPs assembled onto CdS NRs, the photoinduced electrons accumulate on the Fe_2O_3 . The local Coulomb attraction is generated to promote the holes transfer away from CdS. Meanwhile, the photocatalytic durability is prolonged.

is depicted in Fig. 1. Its formation is attributed to the local accumulation of the electrons on Fe_2O_3 , which originates from the local unbalance of migration of photogenerated holes and electrons. Furthermore, the general function of Coulomb attraction strategy for $Zn_{0.5}Cd_{0.5}S$ photocatalyst was also confirmed, demonstrating its potential to serve on metal sulfides.

2. Experimental methods

2.1. Synthesis of photocatalyst

CdS NRs was synthesized according to previously published procedure [34]. For comparison, the CdS NRs with varied content of Fe_2O_3 NPs were prepared by photochemical metal-organic deposition (PMOD), using ferric acetylacetonate ($Fe(Ac)_3$) as the starting material, and labeled as FCS-5, FCS-10, FCS-15, FCS-20. For a typical synthesis, 100 mg of CdS NRs and 10 ml of different concentration of $Fe(Ac)_3$ ethanol solution (0, 2.2, 4.4, 6.6 and 8.8 mg ml^{-1}) were dispersed into 40 ml distilled water. To eliminate the interference of dissolved oxygen in precursor solution, the system was evacuated by vacuum pump, then the suspension was irradiated with 300 W Xenon lamp for 1 h. After PMOD, the prepared powder of Fe_2O_3 /CdS NRs were collected by centrifugation, purged three times by distilled water and ethanol respectively, and were dried at 60°C for over 12 h in a vacuum oven to evaporate the solvent.

For the comparison of optimal Fe_2O_3 /CdS NRs, 2.4 wt% Ni and Pt loaded CdS NRs were prepared following photochemical deposition, according to previously published procedure [33,35]. $Zn_{0.5}Cd_{0.5}S$ were prepared according to previously published procedures [36]. Fe_2O_3 / $Cd_{0.5}Zn_{0.5}S$ was prepared by PMOD under the similar condition.

2.2. Materials characterizations

XRD analysis (D/MAX 2550 VB/PC) was collected to study the crystal structure. The surface elements content and valence were studied by XPS measurements (ESCALAB 250Xi). The C 1s peak at 284.6 eV was adopted as an internal reference in this work. SEM (HITACHI S4800) was used to study the morphology of the as prepared samples. The lattice fringe, structures and SAED of the as prepared

samples were analyzed by TEM (JEM 2100, 200 kV). Samples were prepared by dispersing fine powders in ethanol using sonication, followed by depositing a drop of solution onto a holey, carbon-coated Cu grid. FTIR spectroscopy was carried out using a Jasco FTIR-4100 (Japan) spectrometer. UV–vis diffuse reflection spectra were carried out with a UV–vis spectrophotometer (CARY 500). The contents of elements Cd and Fe in the varied samples were analyzed by ICP-AES (Varian 710ES). To test the recombination of photoinduced electron-hole pairs, PL spectra were obtained by an Edinburgh Instruments (FLSP 920) system operated at room temperature. TRPL spectra were obtained on Fluorolog-3 (HORIBA), to measure the precise life time of photoinduced charges. Fe K-edge XANES was performed on the 1W1B beamline of the Beijing Synchrotron Radiation Facility, China, operated at $\sim 200 \text{ mA}$ and $\sim 2.5 \text{ GeV}$. Fe foil, FeO and Fe_2O_3 were used as the reference samples and measured in the transmission mode, and the initial and used Fe_2O_3 /CdS photocatalyst were measured in fluorescence mode. Transient photocurrent response and EIS were performed using an electrochemical station (CHI 660E) in a three-electrode setup with Ag/AgCl/KCl (3.5 M) electrodes as a reference electrode, Pt foil as a counter electrodes. And the mixed ethanol aqueous solutions (20% v/v) was chosen as the supporting electrolyte. The working electrode was prepared as follows: 2 mg of catalyst and 20 μl nafion solution (5 wt%) were dispersed in 500 μl ethanol aqueous solution (20% v/v) by 30 min ultrasound to form a homogeneous slurry. And then 20 μl slurry was spread on a $1.0 \times 2.5 \text{ cm}$ fluorine-doped tin oxide (FTO) glass substrate whose side part was previously protected by Scotch tape to ensure an active area of approximately 1.0 cm^2 . The resulting electrodes were dried in the air. Transient photocurrent response measurements were performed under irradiation condition using a solar light simulator (Oriel, 91160, AM 1.5 globe) with light intensity of 100 mW cm^{-2} at a bias potential of $-0.6 \text{ V vs. Ag/AgCl}$.

2.3. Photocatalytic tests

The solar-driven H_2 -evolution reactions operated to estimate the activities of the photocatalysts were carried out in a glass gas-closed-circulation system (CEL-SPH2N, CEAULight, China) with a top irradiation-type reaction vessel (LabSolar H_2). In a typical photocatalytic H_2 -evolution reaction, 25 mg photocatalyst was dispersed in 50 ml of aqueous solution containing ethanol (20% v/v) as holes scavenger. 300 W Xenon lamp (CEL-HXBF300) equipped with an ultraviolet cutoff filter was operated to provide visible light with $> 420 \text{ nm}$. The amount of evolved H_2 was analyzed by an online gas chromatograph/equipped with a TCD detector, using Ar carrier gas, and monitored every 30 min in order to determine the H_2 evolution rate. The suspension was put in ultrasonic bath for 10 min before the reaction and stirred during the test procedure in order to eliminate sedimentation. After evacuation by vacuum pump, air hardly can be detected in the system. To decide the photocatalytic stability of the sample of FCS-15, the long-term photocatalytic H_2 evolution experiment was conducted for 6 days.

3. Results and discussion

The Fe_2O_3 /CdS NRs samples prepared by PMOD using various contents of iron precursor are labeled as FCS-5, FCS-10, FCS-15 and FCS-20 (see details in Section 2). As shown in Fig. S1, the X-ray diffraction (XRD) reveals that the strong diffraction peaks are assigned well to the hexagonal CdS (PDF# 77-2306). The peaks of Fe_2O_3 can be hardly observed in the XRD patterns, mainly due to its low contents. The precise amount of Fe_2O_3 was determined by inductively coupled plasma-atomic emission spectroscopy (ICP-AES), as shown in Table S1. The results reveal the highest loading amount is 2.40 wt%, observed in the FCS-15. It is worth noting that the photocatalyst CdS could be easily coated with organic ligands, which either increase or decrease the photocatalytic performance [33,37]. Therefore, to eliminate the additional ligands coating on CdS NRs surface after PMOD, the samples

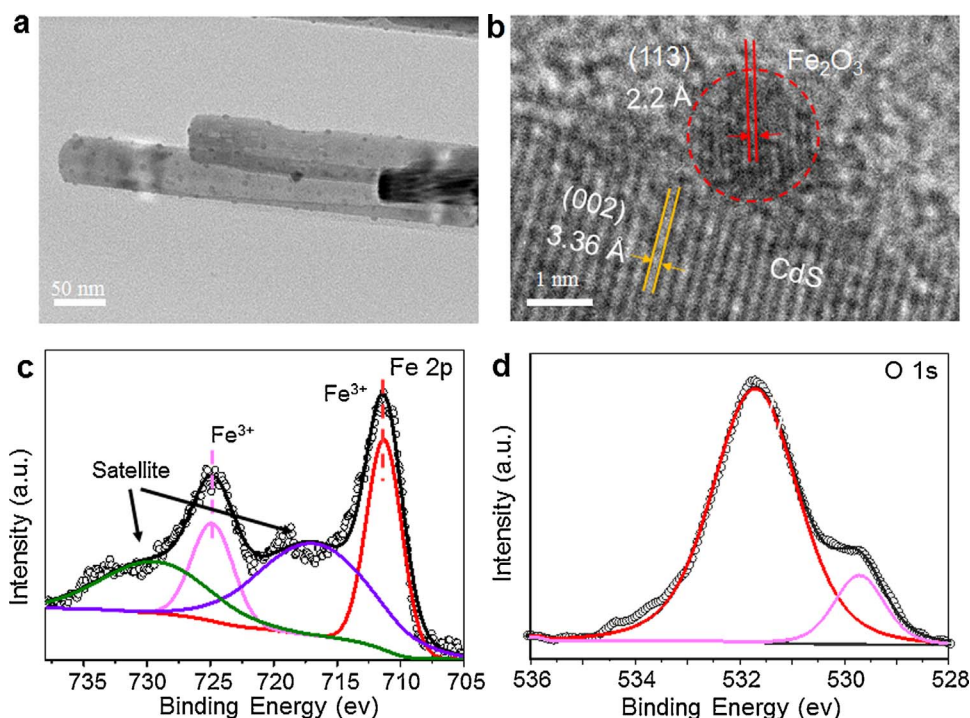


Fig. 2. (a) TEM image for FCS-15; (b) HRTEM image for the interface between CdS NRs and Fe_2O_3 NPs; XPS spectra of FCS-15 for (c) Fe 2p and (d) O 1s.

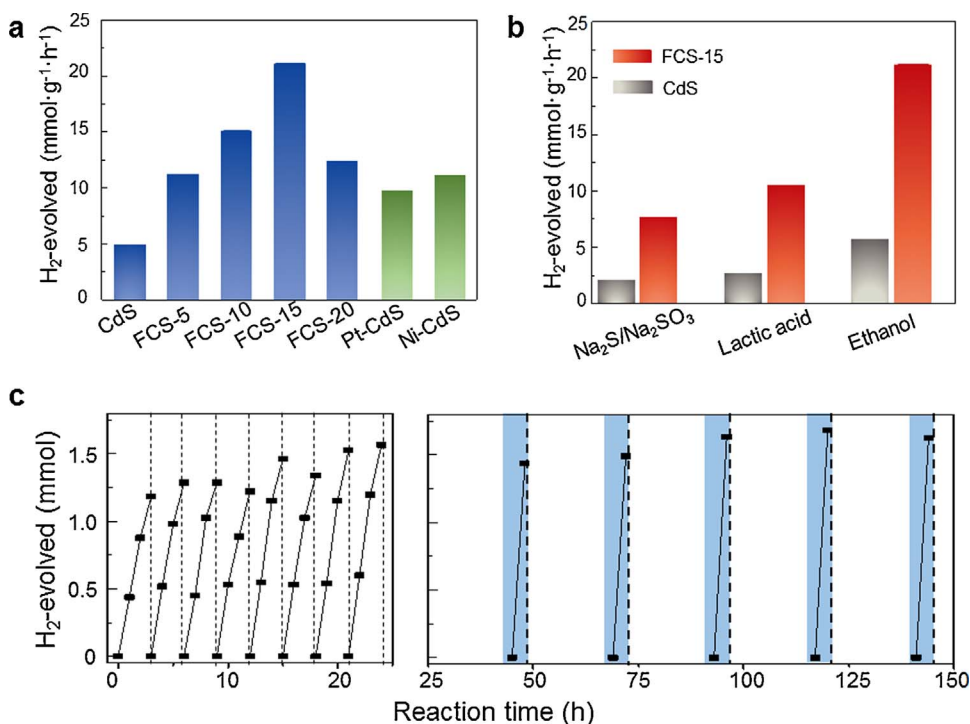


Fig. 3. (a) Photocatalytic H_2 -evolved rate of pure CdS, FCS-5, FCS-10, FCS-15 and FCS-20 under visible light irradiation ($\lambda > 420$ nm) with sacrificial agent; (b) Photocatalytic activity of pure CdS and FCS-15 with different sacrificial agent ($\text{Na}_2\text{S}/\text{Na}_2\text{SO}_3$, lactic acid and ethanol) under visible light irradiation ($\lambda > 420$ nm); (c) Long-term photocatalytic H_2 evolution for FCS-15 under visible light irradiation with ethanol as sacrificial agent in the alkaline solution.

have been carefully washed (see details in Section 2). Fourier transform infrared spectroscopy (FTIR) analysis shows no obvious differences between CdS and FCS-15 (Fig. S2), demonstrating the absence of residual ligands on the FCS-15 photocatalyst surface.

The morphologies of pure CdS and FCS-15 samples were studied by microscopic observations. Scanning and transmission electron microscopy (SEM and TEM) images reveal that pure CdS features the nanorod structure with a mean diameter of ~ 40 nm and length of ~ 5 μm (Fig. S3). Besides, the selected-area electron diffraction (SAED) image (Fig. S3) shows ordered spots, further confirming the well-defined crystalline structure. After photodeposition, the nanorod structure of CdS is merely

altered (Fig. S4a). The corresponding SEM elemental mapping images illuminate the existence of element Fe (Fig. S4b), which agrees with ICP-AES analysis. Fig. 2a shows that Fe_2O_3 with a mean particle size of approximately 2 nm is loaded onto CdS NRs surface. In addition, the lattice distance of 3.36 and 2.2 Å can be found in the high-resolution TEM (HRTEM) image (Fig. 2b), which are assigned to the (002) plane of hexagonal CdS and (113) plane of Fe_2O_3 , respectively [14,38].

To analyze the surface elemental composition and valence state of the as-prepared $\text{Fe}_2\text{O}_3/\text{CdS}$ NRs, X-ray photoelectron spectroscopy (XPS) measurement was carried out. The peaks in XPS survey scanned spectrum confirm the presence of Cd, S, Fe, O and C elements,

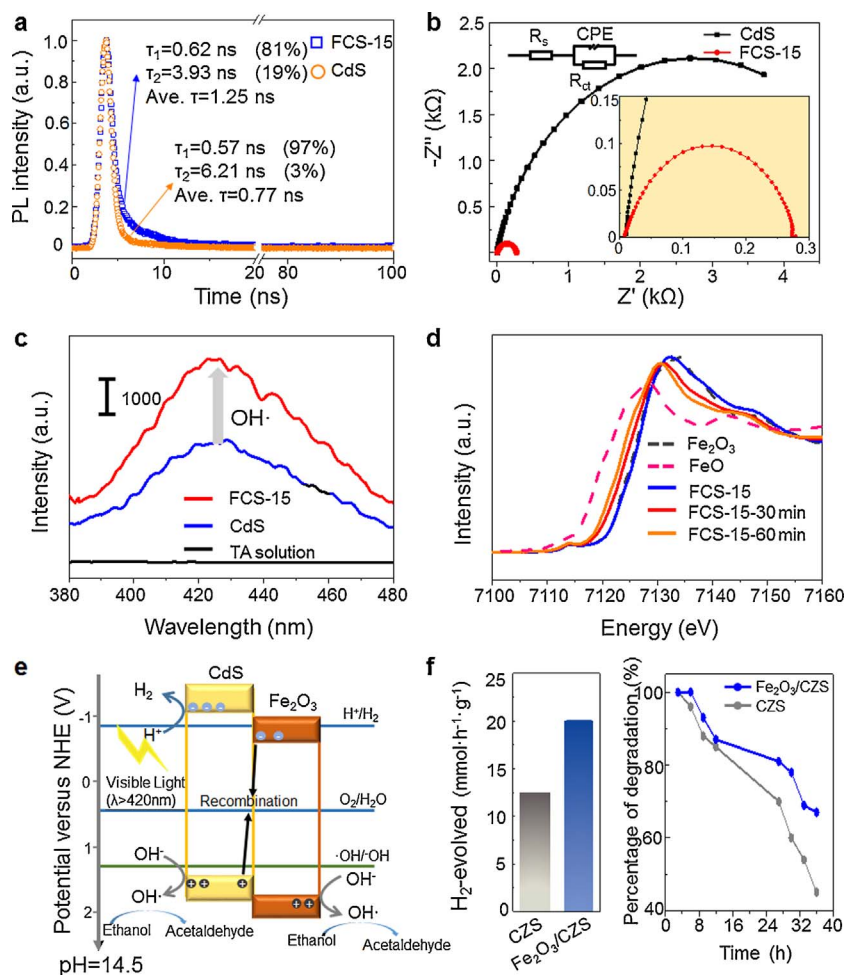


Fig. 4. (a) Time-resolved PL spectra for the samples of CdS and FCS-15 (excitation at 400 nm, emission at 525 nm); (b) Nyquist plots for pristine CdS NRs and FCS-15 measured at ethanol mixture solution; (c) Comparison of OH radical formation illustrated by photoluminescence (PL) spectra of 2-hydroxyterephthalic acid (product of the reaction of the radical with terephthalic acid) taken after 3 h of illumination. The excitation wavelength was 320 nm; (d) In-situ Fe K-edge XANES spectra of FCS-15 under different time irradiation and controlled samples; (e) The proposed photocatalytic mechanisms of Fe₂O₃/CdS photocatalysis; (f) Photocatalytic activity and stability of Cd_{0.5}Zn_{0.5}S.

indicating the inexistence of other elements (Fig. S5). The XPS spectrum of Cd 3d shows two peaks at Cd 3d_{5/2} (405.25 eV) and Cd 3d_{3/2} (412.0 eV), together with the S 2p_{3/2} (161.6 eV) and S 2p_{1/2} (162.6 eV) [39], which are assigned to the Cd²⁺ and S²⁻ species in CdS, respectively (Fig. S6a and b). In the XPS spectrum for Fe 2p region, two major peaks at binding energy of 711.3 and 724.6 eV (Fig. 2c), with their satellites at 718.2 and 730.2 eV, belong to Fe³⁺ [40]. As shown in Fig. 2d, two peaks of O 1s at 529.7 and 531.7 eV are attributed to the hydroxyl group on the CdS NRs surface and the lattice oxygen in the Fe₂O₃ crystalline lattice, respectively [39,40]. Thus, the XPS results further testify that Fe₂O₃ NPs are loaded on the surface of well-fine CdS NRs via PMOD.

The photocatalytic H₂ evolution rate of Fe₂O₃/CdS NRs was measured in 5.0 M NaOH aqueous solution containing 20 vol% ethanol as the sacrificial reagent under visible light illumination ($\lambda > 420$ nm). NaOH can produce the redox couple OH⁻/OH \cdot operating as a shuttle to offer an efficient transfer way for photogenerated holes from CdS surface to the scavenger [33]. The results are summarized in Fig. 3a. The highest H₂ evolution rate is observed for sample FCS-15, which is up to 20.7 mmol g⁻¹ h⁻¹ (approximately 5 times higher than that of pure CdS NRs). Remarkably, the Fe₂O₃/CdS NRs exhibits a higher activity compared to other controlled metal co-catalysts (such as Pt and Ni) loaded on CdS NRs. Additionally, the photocatalytic activities of Fe₂O₃/CdS NRs synthesized via different iron resources are shown in Fig. S7. As compared with FeCl₃ and Fe(NO₃)₃, Fe(Ac)₃ can prevent Fe³⁺ from reacting with S²⁻ on the CdS surface to form Fe₂S₃, which decreases the photocatalytic performance. To our best knowledge, the formation of metal oxide can be influenced by pH. Thus, the photocatalytic activities of Fe₂O₃/CdS NRs synthesized via different pH conditions are

investigated (Fig. S8). To identify the wide applications of Fe₂O₃/CdS NRs on other sacrificial reagents and varied pH, the H₂ evolution rates of FCS-15 in Na₂S/Na₂SO₃ and lactic acid aqueous solution were also investigated (Fig. 3b). The photocatalytic activity increases 4.0 times in Na₂S/Na₂SO₃ solution, 4.2 times in lactic acid, as comparison with those of pristine CdS NRs. These results suggest that Fe₂O₃/CdS NRs exhibits increasing photocatalytic H₂ evolution rate under both acidic and alkaline conditions. Overall, it is clear that Fe₂O₃ NPs can greatly enhance the photocatalytic activity of CdS NRs.

The rapid decay of photocatalytic activity is considered as the most severe drawback for metal sulfides materials. It is highly desirable but challenging to enhance their photocatalytic durability. After assembling Fe₂O₃ NPs onto CdS NRs, the photocatalytic stability reveals a tremendously prolonging time over 6 days without obvious decrease (Fig. 3c). Contrarily, pristine CdS NRs shows poor photocatalytic stability with less than 12 h (Fig. S9). Thus, Fe₂O₃ NPs efficiently protect CdS NRs from photocorrosion during the photocatalytic process, leading to an excellent photocatalytic stability. This result implies that the holes in CdS can be expelled after loading Fe₂O₃ NPs. Moreover, the optimal Fe₂O₃/CdS photocatalyst in our work displays one of the best durability (Table S2). To detect the change of FCS-15 after photocatalytic H₂ evolution, the XRD and XPS analyses of the used FCS-15 sample were carried out. As shown in Fig. S10, the peaks of the used FCS-15 match well with those of the initial, revealing the stability of CdS crystal structure. The XPS spectra of Fe, O, Cd and S are depicted in Fig. S11. The Cd 3d, S 2p and O 1s spectra of the used FCS-15 are all similar compared to those of FCS-15. It is mentioning that the peaks of a characteristic doublet of Fe 2p in used FCS-15 are found to shift to lower binding energy, indicating the decreased valence of Fe element.

Those results verify the consistence of CdS crystal structure due to the protection of Fe₂O₃, revealing the excellent photocatalytic stability of Fe₂O₃/CdS system.

Further, the optical and electronic properties of the CdS NRs and FCS-15 were analyzed. Ultraviolet-visible (UV-vis) absorption spectra were conducted to measure the optical absorption properties (Fig. S12). The absorption edge of pristine CdS NRs is shown at around 520 nm. A weak absorption enhancement in the spectral region of 520 nm can be observed from FCS-15, which probably arises from the absorption of Fe₂O₃ NPs. Additionally, the photoelectrochemical performances of bare CdS NRs and FCS-15 were conducted in the mixed solution (0.25 mM Na₂S and 0.35 mM Na₂SO₃) under visible light irradiation. As shown in Fig. S13, the sample FCS-15 shows higher photocurrent intensity than the pure CdS NRs, revealing the promoted separation efficiency of charge carriers in FCS-15. This result indicates the enhanced photocatalytic activity of FCS-15.

To understand the reason for prolonging photocatalytic stability of Fe₂O₃/CdS NRs, photoluminescence (PL) and time-resolved photoluminescence (TRPL) analysis were performed. A broad emission peak in the sample CdS NRs and FCS-15 centers at around 525 nm (Fig. S14). It can be observed that the PL intensity of the Fe₂O₃/CdS NRs decreases, compared with that of pristine CdS NRs. It derives from the fast transfer of holes away from CdS NRs, which suppresses the electron-hole recombination [41]. Furthermore, the fast holes transfer has also been confirmed by the TRPL spectra. As shown in Fig. 4a, Fe₂O₃/CdS NRs shows an increased intensity-average PL life-times (τ). After removal of the holes, the electrons are liberated from the Coulomb attraction, leading to increased charge lifetime. Therefore, the PL and TRPL analyses demonstrate the fast holes migration in Fe₂O₃/CdS NRs. After fast moving the holes away from intrinsic CdS NRs, the photocorrosion can be efficiently hindered, and the photocatalytic durability is thus dramatically prolonged.

To further proof the fast holes transfer, electrochemical impedance spectra (EIS) and the characteristic PL were carried out. As shown in Fig. 4b, FCS-15 exhibits much smaller semicircle in the middle-frequency region, compared with that of pure CdS NRs, indicating its fast interfacial charge transfer between the photocatalyst and the scavenger [42]. Furthermore, the characteristic PL of 2-hydroxyterephthalic acid, a product of the reaction of terephthalic acid (TA) with OH radical, was utilized to test the amount of hydroxyl radical. As reported by Thomas Simon and co-workers, the generating rate of hydroxyl radical reflects the holes transfer rate from CdS crystal lattice to the scavenger [32]. After illuminating for 3 h, significantly more OH radicals are formed from sample FCS-15, compared with that of pristine CdS NRs (Fig. 4c). It is demonstrated that the holes transfer from CdS crystal lattice to the scavenger is greatly accelerated, which may derive from the Coulomb attraction between CdS and Fe₂O₃.

To perceive the formation of Coulomb attraction, the valence change of iron element in FCS-15 was examined by in situ Fe K-edge XANES. The XANES analyses were performed under visible light irradiation with ethanol as sacrificial agent in the alkaline solution. In Fig. 4d, for Fe K-edge XANES spectra, FCS-15 matches with the reference sample Fe₂O₃, indicating Fe³⁺ in the FCS-15. Nevertheless, after illuminating for 30 and 60 min, the white-line peaks both show a slight decrease, but higher than that of the reference sample FeO. The results indicate the iron element continuously keeps a valence state between Fe²⁺ and Fe³⁺ under reaction condition. To our best knowledge, the small size of Fe₂O₃ NPs shorten the range of photogenerated charge conductivity, which improves the mobility of holes to surface oxidation site [43,44]. Additionally, as outstanding water oxidation material, Fe₂O₃ favors the process of the oxidation reaction of the photoinduced holes [45,46], leading to the rapid consumption of holes. However, thermodynamically, the electrons on the conduction band (CB) of Fe₂O₃ are not favorable for the water reduction [47]. Therefore, the photogenerated holes in the Fe₂O₃ NPs can be rapidly consumed by the sacrificial reagent. In contrary, the consumption of the holes in CdS

NRs is relatively slow, due to the long transfer distance in large crystal size and the steric barrier of the surface ligands. As a result, the electrons are bond to accumulate on the Fe₂O₃, causing the decrease of Fe valence. The Coulomb attraction is considered as a universal signature between hole and electron. Subsequently, Coulomb attraction between the Fe₂O₃ concentrated electrons and CdS holes is introduced, which accelerates the CdS holes transfer. Although the CB electrons from CdS can transfer to Fe₂O₃ in thermodynamics, these electrons will further act as the local Coulomb attractor to recombine with holes instead of reducing protons into hydrogen, because the CB of Fe₂O₃ is more positive than the potential of water reduction. Additionally, the enhanced photocatalytic activity indicate CB electrons from CdS trend to reduce water, rather than transfer to Fe₂O₃.

On the basis of these observation, the mechanistic details of photocatalytic charge carriers migration are illustrated in Fig. 4e. The simultaneous solar light reflections of CdS and Fe₂O₃ are allowed, which is identified by the UV-vis analysis. The photoinduced holes on the valence band (VB) of Fe₂O₃ NPs are rapidly consumed by the sacrificial agent. Meanwhile, the electrons on the CB of Fe₂O₃ tend to accumulate. However, the consumption of the holes in CdS is relatively slow. Then strong local Coulomb attraction emerges between the Fe₂O₃ concentrated electrons and CdS holes. Thus, under attraction force, the CdS holes can be rapidly transferred to Fe₂O₃, and recombine with the electrons on the CB of Fe₂O₃. Consequently, the photostability is tremendously enhanced. In addition, the electrons on the CB of CdS become free [33], which demonstrates the outstanding photocatalytic activity of Fe₂O₃/CdS NRs. To demonstrate the potential application of the Coulomb attraction strategy, Fe₂O₃ NPs were loaded onto the Zn_{0.5}Cd_{0.5}S via the similar method, and its XRD pattern and SEM images are shown in Fig. S15. The photocatalytic activity and stability of Fe₂O₃/Zn_{0.5}Cd_{0.5}S both increase with respect to that of pristine Zn_{0.5}Cd_{0.5}S (Fig. 4f). This inspiring result convincingly demonstrates that this strategy shows wide applications in a variety of metal sulfides photocatalysts for photocatalytic H₂ evolution.

4. Conclusions

In summary, we report a strategy of strong local Coulomb attraction to effectively stimulate the transfer of photoinduced holes. Remarkably, as holes attraction unit, Fe₂O₃ NPs endow CdS NRs with excellent photocatalytic durability of 6 days, up to 132 h longer as compared with that of rare CdS NRs, which is among the best stable CdS based photocatalysts. Meanwhile, Fe₂O₃/CdS photocatalyst exerts an outstanding H₂ evolution rate of 20.7 mmol g⁻¹ h⁻¹. Further application of Fe₂O₃ NPs on Zn_{0.5}Cd_{0.5}S photocatalyst validly testifies the extensive applications of this strategy for metal sulfides. In a wider range of photocatalysis, this Coulomb attraction strategy can control the mobility of charge carriers for effective catalytic activity and as such indicates a feasible way to develop high-active photocatalysts for overall water splitting.

Author contributions

The manuscript was written through contributions of all authors. All authors have given approval to the final version of the manuscript.

Conflict of interest

The authors declare no competing financial interests.

Acknowledgments

This work was financially supported by National Natural Science Foundation of China (21573068 and 21603073), Program of Shanghai Subject Chief Scientist (15XD1501300), Fundamental Research Funds for the Central Universities (222201514303 and 222201714001),

China Postdoctoral Science Foundation Funded Project (2016M591615 and 2016M601523), National Postdoctoral Program for Innovative Talents (BX201600050), Shanghai Sailing Program (17YF1402900) and “Chen Guang” project supported by Shanghai Municipal Education Commission and Shanghai Education Development Foundation (16CG31). The authors also thank the crew of 1W1B beamline of Beijing Synchrotron Radiation Facility for the constructive assistance in the XAFS measurements and data analyses.

Appendix A. Supplementary data

Supplementary data associated with this article can be found, in the online version, at <http://dx.doi.org/10.1016/j.apcatb.2017.09.012>.

References

- [1] Z. Han, F. Qiu, R. Eisenberg, P.L. Holland, T.D. Krauss, *Science* 338 (2012) 1321–1324.
- [2] X. Chen, L. Liu, P.Y. Yu, S.S. Mao, *Science* 331 (2011) 746–750.
- [3] T. Hisatomi, J. Kubota, K. Domen, *Chem. Soc. Rev.* 43 (2014) 7520–7535.
- [4] A. Kudo, Y. Miseki, *Chem. Soc. Rev.* 38 (2009) 253–278.
- [5] J. Song, H. Zhao, R. Sun, X. Li, D. Sun, *Energy Environ. Sci.* 10 (2017) 225–235.
- [6] Z. Bai, X. Yan, Y. Li, Z. Kang, S. Cao, Y. Zhang, *Adv. Energy Mater.* 6 (2016) 1501459.
- [7] J. Yu, Y. Yu, P. Zhou, W. Xiao, B. Cheng, *Appl. Catal. B: Environ.* 156 (2014) 184–191.
- [8] C. Han, Z. Chen, N. Zhang, J.C. Colmenares, Y.-J. Xu, *Adv. Funct. Mater.* 25 (2015) 221–229.
- [9] H. Yu, X. Huang, P. Wang, J. Yu, *J. Phys. Chem. C* 120 (2016) 3722–3730.
- [10] H.-W. Tseng, M.B. Wilker, N.H. Damrauer, G. Dukovic, *J. Am. Chem. Soc.* 135 (2013) 3383–3386.
- [11] H. Tada, T. Mitsui, T. Kiyonaga, T. Akita, K. Tanaka, *Nat. Mater.* 5 (2006) 782–786.
- [12] F.-X. Xiao, J. Miao, B. Liu, *Mater. Horiz.* 1 (2014) 259.
- [13] J. Zhang, Z. Zhu, Y. Tang, K. Müllen, X. Feng, *Adv. Mater.* 26 (2014) 734–738.
- [14] Y. Huang, Y. Liu, D. Zhu, Y. Xin, B. Zhang, *J. Mater. Chem. A* 4 (2016) 13626–13635.
- [15] L.J. Zhang, S. Li, B.K. Liu, D.J. Wang, T.F. Xie, *ACS Catal.* 4 (2014) 3724–3729.
- [16] T.K. Van, L.Q. Pham, D.Y. Kim, J.Y. Zheng, D. Kim, A.U. Pawar, Y.S. Kang, *ChemSusChem* 7 (2014) 3505–3512.
- [17] X. Wang, G. Liu, L. Wang, Z.-G. Chen, G.Q. (Max) Lu, H.-M. Cheng, *Adv. Energy Mater.* 2 (2012) 42–46.
- [18] Z.B. Yu, Y.P. Xie, G. Liu, G.Q. (Max) Lu, X.L. Ma, H.-M. Cheng, *J. Mater. Chem. A* 1 (2013) 2773–2776.
- [19] Y.P. Xie, Z.B. Yu, G. Liu, X.L. Ma, H.-M. Cheng, *Energy Environ. Sci.* 7 (2014) 1895–1901.
- [20] D. Jiang, Z. Sun, H. Jia, D. Lu, P. Du, *J. Mater. Chem. A* 4 (2016) 675–683.
- [21] Y. Shemesh, J.E. Macdonald, G. Menagen, U. Banin, *Angew. Chem. Int. Ed.* 50 (2011) 1185–1189.
- [22] H. Yan, J. Yang, G. Ma, G. Wu, X. Zong, Z. Lei, J. Shi, C. Li, *J. Catal.* 266 (2009) 165–168.
- [23] S. Zhang, Q. Chen, D. Jing, Y. Wang, L. Guo, *Int. J. Hydrogen Energy* 37 (2012) 791–796.
- [24] K.P. Acharya, R.S. Khayzer, T. O'Connor, G. Diederich, M. Kirsanova, A. Klinkova, D. Roth, E. Kinder, M. Imboden, M. Zamkov, *Nano Lett.* 11 (2011) 2919–2926.
- [25] T. O'Connor, M.S. Panov, A. Mereshchenko, A.N. Tarnovsky, R. Lorek, D. Perera, G. Diederich, S. Lambright, P. Moroz, M. Zamkov, *ACS Nano* 6 (2012) 8156–8165.
- [26] W. Bi, L. Zhang, Z. Sun, X. Li, T. Jin, X. Wu, Q. Zhang, Y. Luo, C. Wu, Y. Xie, *ACS Catal.* 6 (2016) 4253–4257.
- [27] J. Chen, X.-J. Wu, L. Yin, B. Li, X. Hong, Z. Fan, B. Chen, C. Xue, H. Zhang, *Angew. Chem. Int. Ed.* 54 (2015) 1210–1214.
- [28] J. Ran, G. Gao, F.-T. Li, T.-Y. Ma, A. Du, S.-Z. Qiao, *Nat. Commun.* 8 (2017) 13907.
- [29] L. Shang, B. Tong, H. Yu, G.I.N. Waterhouse, C. Zhou, Y. Zhao, M. Tahir, L.-Z. Wu, C.-H. Tung, T. Zhang, *Adv. Energy Mater.* 6 (2016) 1501241.
- [30] M. Liu, D. Jing, Z. Zhou, L. Guo, *Nat. Commun.* 4 (2013) 2278.
- [31] L. Ma, K. Chen, F. Nan, J.-H. Wang, D.-J. Yang, L. Zhou, Q.-Q. Wang, *Adv. Funct. Mater.* 26 (2016) 6076–6083.
- [32] I. Vamvakakis, B. Liu, G.S. Armatas, *Adv. Funct. Mater.* 26 (2016) 8062–8071.
- [33] T. Simon, N. Bouchonville, M.J. Berr, A. Vaneski, A. Adrović, D. Volbers, R. Wyrwich, M. Döblinger, A.S. Susha, A.L. Rogach, F. Jäkel, J.K. Stolarczyk, J. Feldmann, *Nat. Mater.* 13 (2014) 1013–1018.
- [34] Z.J. Sun, H.F. Zheng, J.S. Li, P.W. Du, *Energy Environ. Sci.* 8 (2015) 2668–2676.
- [35] Y. Wang, Y. Wang, R. Xu, *J. Phys. Chem. C* 117 (2013) 783–790.
- [36] J. Song, H. Zhao, R. Sun, X. Li, D. Sun, *Energy Environ. Sci.* 10 (2017) 225–235.
- [37] C.M. Chang, K.L. Orchard, B.C.M. Martindale, E. Reisner, *J. Mater. Chem. A* 4 (2016) 2856–2862.
- [38] L. Li, Y. Yu, F. Meng, Y. Tan, R.J. Hamers, S. Jin, *Nano Lett.* 12 (2012) 724–731.
- [39] P.-Y. Kuang, P.-X. Zheng, Z.-Q. Liu, J.-L. Lei, H. Wu, N. Li, T.-Y. Ma, *Small* 12 (2016) 6735–6744.
- [40] L. Wang, H. Yang, X. Liu, R. Zeng, M. Li, Y. Huang, X. Hu, *Angew. Chem. Int. Ed.* 56 (2017) 1105–1110.
- [41] B. Liu, X. Li, Q. Zhao, J. Ke, M. Tadó, S. Liu, *Appl. Catal. B: Environ.* 185 (2016) 1–10.
- [42] T. Li, X. Li, Q. Zhao, Y. Shi, W. Teng, *Appl. Catal. B: Environ.* 156–157 (2014) 362–370.
- [43] S. So, P. Schmuki, *Angew. Chem. Int. Ed.* 52 (2013) 7933–7935.
- [44] C.W. Wang, S. Yang, W.Q. Fang, P. Liu, H. Zhao, H.G. Yang, *Nano Lett.* 16 (2016) 427–433.
- [45] Y. Yang, M. Forster, Y. Ling, G. Wang, T. Zhai, Y. Tong, A.J. Cowan, Y. Li, *Angew. Chem. Int. Ed.* 55 (2016) 3403–3407.
- [46] P. Zhang, T. Wang, X. Chang, L. Zhang, J. Gong, *Angew. Chem. Int. Ed.* 55 (2016) 5851–5855.
- [47] S. Hussain, S. Hussain, A. Waleed, M.M. Tavakoli, Z. Wang, S. Yang, Z. Fan, M.A. Nadeem, *ACS Appl. Mater. Interfaces* 8 (2016) 35315–35322.